Estimation of Fluorescence Lifetimes Via Rotational Invariance Techniques

Hongqi Yu*, Rebecca Saleeb, Paul Dalgarno, and David Day-Uei Li*

***Abstract*—Estimation of signal parameters via rotational invariance techniques is a classical algorithm widely used in array signal processing for direction-of-arrival estimation of emitters. Inspired by this method, a new signal model and new fluorescence lifetime estimation via rotational invariance techniques (FLERIT) were developed for multiexponential fluorescence lifetime imaging (FLIM) experiments. The FLERIT only requires a few time bins of a histogram generated by a time-correlated single-photon counting FLIM system, greatly reducing the data throughput from the imager to the signal processing units. As a noniterative method, the FLERIT does not require initial conditions, prior information nor model selection that are usually required by widely used traditional fitting methods, including nonlinear least square methods or maximum-likelihood methods. Moreover, its simplicity means it is suitable for implementations in embedded systems for real-time applications. FLERIT was tested on synthesized and experimental fluorescent cell data showing the potentials to be widely applied in FLIM data analysis.**

***Index Terms*—Fluorescence lifetime imaging microscopy (FLIM), fluorescence microscopy, time-correlated single-photon counting (TCSPC), time-resolved imaging.**

I. Introduction

FLUORESCENCE lifetime imaging (FLIM) is a powerful tool to study the microstructure and microenvironments of molecules. FLIM has been widely used throughout modern microscopy, including in the material sciences, biology, chemical analysis, and even for clinical diagnosis. Different from traditional fluorescence intensity imaging, which only provides geometric information of tissues or materials, FLIM measures the inherent lifetime of a fluorescent molecule (fluorophore) as it undergoes radiative absorption and subsequent fluorescent relaxation. As the fluorescence lifetime is sensitive to the environment, FLIM can be a good indicator to show how the fluorophore interacts with its microenvironment. Examples include imaging physiological or electrochemical parameters, such as Ca^{2+}, pH, and pO2 [1]–[5]. When combined with fluorescence resonance energy transfer (FRET) [6]–[8] FLIM is the most robust method to study protein–protein interactions [1], [2], premalignant lesions [3], molecular metabolism [4], and drug-targeting efficacy [5]. However, despite the potential and significant impact of FLIM, primarily in the biological sciences, estimation of the fluorescence lifetimes remains a significant challenge, particularly with low photon counts systems such as in rapid live cell imaging. This is becoming increasingly demanding with the development of novel CMOS SPAD array-based widefield FLIM systems, which can generate significant volumes of data [9]–[11]. In this paper, we present a new, rapid, and robust method of extracting lifetime information that requires no prior information on the lifetime components.

There are different FLIM algorithms, mainly in two categories: the time-domain (TD) and frequency-domain (FD) approaches. FD FLIM mostly uses intensified CCDs synchronized to a modulated excitation source for widefield imaging [12]–[15]. The acquisition time is typically a few seconds, but fitting methods are required to extract the lifetimes which can take several seconds to minutes depending on the accuracy requirements. FD lifetime analysis software is usually iterative based. Furthermore accuracy is limited by the CCD array modulation, with the number of phase images (the time bins) typically between 2 and 20. For the TD systems, on the other hand, a pulsed laser is typically used in conjunction with a single-photon counting detector, such as a PMT or SPAD typical TD FLIM instruments either use 1) a time-correlated single-photon counting (TCSPC) module or 2) a time-gated CCD or SPAD [1], [9], [16]. For a TCSPC system, the measurements of the time delay between the laser pulses and the detected photon are repeated, and a histogram of time delays is accumulated in which the lifetimes are extracted using fitting algorithms [17]. TCSPC has been the gold standard FLIM technique due to its high timing resolution (typically $<$100 ps), and recent developments in multichannel TCSPC systems [18]–[20] further allow much faster acquisition, but the increased data throughput accordingly demand faster fitting strategies [21]. For a time-gated camera, a series of intensity images at different delays are recorded to extract lifetimes. Similar to TCSPC systems, curve-fitting software is used to calculate lifetimes when the number of gates is larger than 5. The limitations of either FLIM systems are robust and rapid lifetime extractions. This study aims to provide rapid lifetime extractions from the lowest photon signal data possible (highest noise) to enable increasingly rapid imaging solutions.

Manuscript received March 4, 2015; revised July 9, 2015 and September 1, 2015; accepted October 9, 2015. Date of publication November 9, 2015; date of current version May 18, 2016. This work was supported by the China Scholarship Council, Royal Society (RG140915), the Medical Research Council (MRC: MR/K01563X/1, MR/K015664/1), and the Biological Sciences Research Council (BBSRC: BB/K016865/1). *Asterisk indicates corresponding author.*

*H. Yu is with the School of Electronic Science and Engineering, National University of Defence Technology, Changsha 410073, China, and also with the Centre for Biophotonics, Strathclyde Institute of Pharmacy and Biomedical Sciences, University of Strathclyde, Glasgow G4 0RE, U.K. (e-mail: 13755132901@163.com).

R. Saleeb and P. Dalgarno are with the Institute of Biological Chemistry, Biophysics and Bioengineering, School of Engineering and Physical Sciences, Heriot-Watt University.

*D. Day-Uei Li is with the Centre for Biophotonics, Strathclyde Institute of Pharmacy and Biomedical Sciences, University of Strathclyde, Glasgow G4 0RE (e-mail: david.li@strath.ac.uk).

Color versions of one or more of the figures in this paper are available online at http://ieeexplore.ieee.org.

Digital Object Identifier 10.1109/TBME.2015.2491364

There are two kind of algorithms mainly employed to obtain accurate fluorescence lifetimes. The first type is the widely used fitting methods, including Bayesian [22], maximum likelihood or maximum entropy [23], method of moments [24]–[26], and promptness ratio method [27]. Although fitting methods are precise, they are limiting as 1) they are computationally intensive, 2) they require prior information about how many lifetime components are contained in the data, and, therefore, model selection is required, and 3) they easily converge to local minima. For realistic experiments, particularly in the low photon regime, it may be difficult to precisely know how many lifetime exponents are in every pixel, and researchers usually need to try or choose a proper data model for accurate fitting. The second method for extracting lifetimes are the nonfitting methods, including the phasor algorithm [28], [29], Prony's method [30], the integral equation method (IEM) [31], the center-of-mass method (CMM) [32]–[35], and rapid lifetime determination [36]–[39]. The phasor method and Prony's method are based on the first-order model. The main criticism of all these techniques seems to be that they are all only good for monoexponentials apart from phasor which may solve biexponentials if you know one component [40]. Gating techniques can be merged with iterative fitting techniques for resolving biexponential decays [27]. Kim *et al*. highlighted the limitations of traditional biexponential maximum-likelihood estimation (MLE) fitting and discussing proper gate width and how the instrumental response function (IRF) affects the estimations. This approach combined gating methods and MLE, and was only demonstrated on datasets of $(\tau_1, \tau_2) = (1.0\text{ ns}, 3, 9\text{ ns})$.

In this paper, we propose a new method of lifetime extraction based on a classical algorithm called estimation of signal parameters via rotational invariance techniques (ESPRIT) [22]. ESPRIT has been widely used in array signal processing for direction-of-arrival estimation of emitters, wireless communications, sonar, and speech signal processing [41]–[43]. Inspired by ESPRIT, we proposed a new signal model and applied this model for estimation of fluorescence lifetime based on rotational invariance techniques, a system we term FLERIT. FLERIT is 1) noniterative, 2) capable of resolving multiexponential decays, 3) able to resolve lifetimes when the measurement-window-to-lifetime ratio is less than 2, and 4) suitable for implementations with embedded hardware for real-time applications. This paper presents the theory (see Section II), and demonstrates the potential through application to both simulated (see Section III) and experimental (Section IV) data.

II. Theory

Similar to previously published literature, we suppose the number of the exponential decays is P without considering the IRF [44]. Following the model proposed by Hall and Selinger [24], the fluorescence intensity density can be expressed in continuous TD as

$$y(t) = \sum_{j=1}^{P} \left(f_{Dj} e^{-t/\tau_j} \right) + n(t)$$

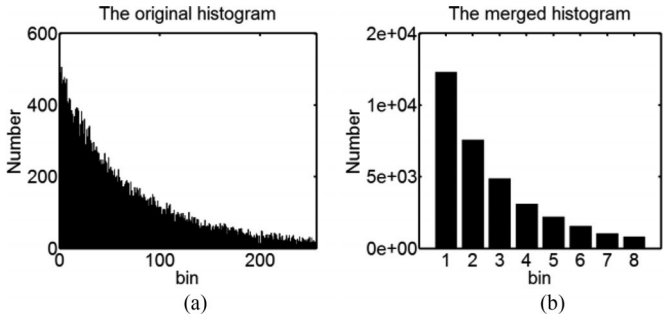

Fig. 1. (a) Original histogram and (b) merged histogram ($K = 8$).

where f_{Dj} and τ_j are the coefficient and the lifetime of the *j*th decay component, respectively, and $n(t)$ is the shot noise.

The *i*th bin of the TCSPC histogram is

$$y(i) = \sum_{j=1}^{P} \left(f_{Dj} e^{-ih/\tau_j} \right) + n(i)$$

where h is the timing resolution of the TCSPC system.

To reduce the computational complexity and noise, we merged B consecutive bins in the original histogram to create a new histogram with K bins as shown in Fig. 1. The histogram in Fig. 1(a) may be obtained by a TCSPC, whereas the one in Fig. 1(b) is obtained by a time-gated FLIM instrument. The photon count in the *i*th bin of the new histogram is

$$x(i) = \sum_{l=1}^{B} y((i-1)B + l), i = 1, 2, 3, \ldots, K.$$

We can arrange the counts from all time bins in the merged histogram as mentioned in [45] as

$$\begin{aligned} X &= (x(1), x(2), \cdots, x(K))^T \\ &= \left(\sum_{l=1}^{B} y(l), \sum_{l=B+1}^{2B} y(l), \cdots, \sum_{l=(K-1)B+1}^{KB} y(l) \right)^T \\ &= \begin{pmatrix} Q_1 & Q_2 & \cdots & Q_P \\ Q_1 e^{-\frac{Bh}{\tau_1}} & Q_2 e^{-\frac{Bh}{\tau_2}} & \cdots & Q_P e^{-\frac{Bh}{\tau_P}} \\ \vdots & \vdots & \ddots & \vdots \\ Q_1 e^{-\frac{(K-1)Bh}{\tau_1}} & Q_2 e^{-\frac{(K-1)Bh}{\tau_2}} & \cdots & Q_P e^{-\frac{(K-1)Bh}{\tau_P}} \end{pmatrix} \\ &\quad \times \begin{pmatrix} f_{D1} \\ f_{D2} \\ \vdots \\ f_{DP} \end{pmatrix} + \begin{pmatrix} m(1) \\ m(2) \\ \vdots \\ m(K) \end{pmatrix} \end{aligned} \quad (1)$$

where

$$m(i) = \sum_{l=1}^{B} n((i-1)B + l)$$

and

$$Q_j = e^{-h/\tau_j}\left(1-e^{-Bh/\tau_j}\right)/\left(1-e^{-h/\tau_j}\right), j=1,\ldots,P.$$

For simplicity, rewrite (1) as

$$X = AS + M. \tag{2}$$

The covariance matrix of (2) [46] can be obtained as

$$R_X = E\left[XX^H\right] = AR_SA^H + \sigma^2 I \tag{3}$$

where $(\cdot)^H$ represents the Hermitian transpose and

$$R_S{=}E\left[SS^H\right].$$

Applying SVD decomposition to R_X, we have

$$\begin{aligned} R_X &= \begin{bmatrix} U_S & U_N \end{bmatrix}\begin{bmatrix} \Sigma_S & O \\ O & \sigma^2 I \end{bmatrix}\begin{bmatrix} U_S^H \\ U_N^H \end{bmatrix} \\ &= U_S\Sigma_S U_S^H + \sigma^2 U_N U_N^H. \end{aligned} \tag{4}$$

As $U_NU_N^H + U_SU_S^H = I$ (U_S contains P eigenvectors corresponding to the P largest eigenvalues of R_X), we can obtain

$$U_S = AR_SA^HU_S\left(\Sigma_S - \sigma^2 I\right)^{-1} = AD \tag{5}$$

where D is a $P \times P$ nonsingular matrix.

Rewriting the right-handed side of (5) as

$$AD = \begin{bmatrix} A_1D \\ C_1D \end{bmatrix} = \begin{bmatrix} C_2D \\ A_2D \end{bmatrix} \tag{6}$$

where C_1 is the last row of A with the dimension $1 \times P$, C_2 is the first row of A with the dimension $1 \times P$, and the dimension of the A_1 and A_2 is $(K-1) \times P$, it is easily seen that the relationship between A_1 and A_2 is

$$A_2 = A_1\Phi \tag{7}$$

where

$$\Phi = \mathrm{diag}\left(e^{-h/\tau_1}, \cdots, e^{-h/\tau_P}\right). \tag{8}$$

Equation (8) shows that all the fluorescence lifetimes are included in the eigenvalues of the matrix Φ. Therefore, once the eigenvalues $\lambda_j, j=1,\ldots,P$, are obtained, all lifetimes can be calculated accordingly by

$$\tau_j = h/\ln\left(\lambda_j\right), j=1,\ldots,P. \tag{9}$$

Similarly, the left-handed side of (5) can be arranged as

$$U_S = \begin{bmatrix} U_1 \\ U_3 \end{bmatrix} = \begin{bmatrix} U_4 \\ U_2 \end{bmatrix} \tag{10}$$

where U_3 is the last row of U_S with the dimension $1 \times P$, U_4 is the first row of U_S with the dimension $1 \times P$, and the dimension of the U_1 and U_2 is $(K-1) \times P$.

From (5)–(7), we have

$$\begin{aligned} U_1 &= A_1D \\ U_2 &= A_2D{=}A_1\Phi D \end{aligned}$$

so

$$U_1D^{-1}\,\Phi D = A_1DU_1D^{-1}\,\Phi D = A_1\Phi D = U_2.$$

Let

$$\Psi = D^{-1}\Phi D \tag{11}$$

then

$$U_1\Psi = U_2. \tag{12}$$

From (11), the eigenvalues of Ψ are equivalent to those of Φ according to the similarity transformation rule [46].

We can calculate Ψ from (12) by applying the LU factorization [46] and its eigenvalues $\lambda_j, (j=1,\ldots,P)$, by the SVD decomposition. The lifetimes can be estimated accordingly by (9). Finally, we can use the following equation to estimate $f_{Dj}, j=1,\ldots,P$, from

$$S = (A^HA)^{(-1)}A^HX. \tag{13}$$

The above outlines the derivation of FLERIT, which can summarize to:

Step 1: Reduce the original histogram into K bins;
Step 2: calculate the correlation matrix of the new histogram using the covariance matrix (3);
Step 3: apply SVD decomposition to R_X, (4), to obtain the signal subspace U_S;
Step 4: obtain Ψ from (10) and (12);
Step 5: calculate the eigenvalues of Ψ by SVD decomposition;
Step 6: obtain the lifetimes by (9) and f_{Dj}, by (13).

The computational burden of the FLERIT is mainly from the SVD decomposition, which is about $O(K^3)$.

III. Simulations on Single-Exponential Decays

We compared the proposed FLERIT with IEM, CMM and Phasor in terms of 1) lifetime dynamic range, 2) photon efficiency, and) K using Monte–Carlo simulations for single-exponential decays. The *F*-value is the normalized precision defined as $F = \sqrt{N_C}\cdot\sigma_\tau/\tau$ [47] ($F=1$ for the ideal case, and $F>1$ or $F \gg 1$ for realistic FLIM algorithms), where N_C is the number of all photons in the histogram and τ the calculated lifetime. To run the simulations, we assume there are 1024 time bins in a histogram and the measurement window $T = 12.5$ ns. The analysis will allow us to optimize the performances of FLERIT.

A. Dynamic Range

We set $K=8$ and the photon number in the first bin is 1000. Fig. 2(a) and (b) show the normalized bias ($\Delta\tau/\tau$) and *F*-value, respectively, in terms of the lifetime. Simulations show that FLERIT has the lowest bias among the four methods. Although CMM shows the lowest *F*-value with the best photon efficiency, its bias is significant when $\tau > 3$ ns and a bias correction measure is required to reduce the bias [35]. IEM has the least optimized range in bias. Phasor shows much less efficient when $\tau > 3$ ns. The optimized region ($F<4$) is from 0.4 to 14 ns for FLERIT, 0.4 to 8.8 ns for IEM, and 0.4 to 4.23 ns for phasor.

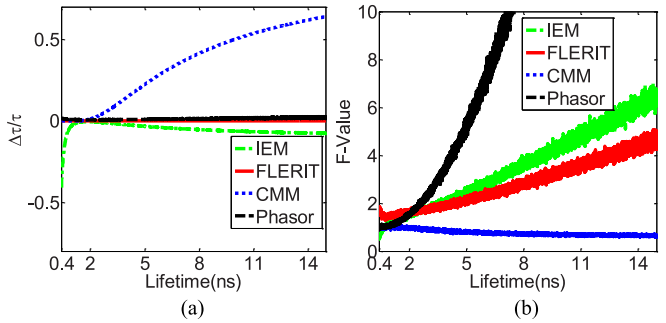

Fig. 2. (a) Bias and (b) F-value plots for different methods in terms of τ (0.4–15 ns). $K = 8$, $T = 12.5$ ns, the photon number in the first bin is 1000, and the number of the time bins is 1024.

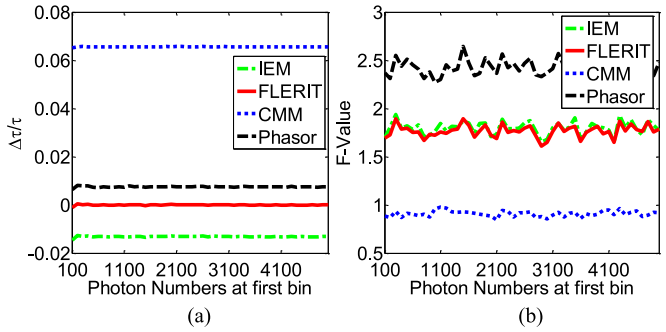

Fig. 3. (a) Bias and (b) F-value plots for different methods in terms of the photon count. $K = 8, \tau = 3$ ns, and the number of the time bins before merging is 1024.

B. Photon Efficiency

The normalized bias and F-value plots in terms of the photon count in the first bin (100–5000) for different methods are shown in Fig. 3(a) and (b). Here, we use $K = 8$ and $\tau = 3$ ns. Again, FLERIT shows the lowest bias. It is interesting that the F-value of FLERIT is similar to IEM, larger than CMM and less than phasor, but CMM has the worst bias performance, unless a bias correction is carried out. Fig. 3(a) shows that both the bias and the normalized F-value should be independent of the photon count as expected.

C. Performances in Terms of K

The normalized bias and F-value plots in terms of K ($4 < K < 32$) for different methods are shown in Fig. 4(a) and (b). Here, we set $\tau = 3$ ns, the photon number in the first bin is 1000, and the number of the time bins is 1024. For FLIRET, the F-value degrades as K increases. FLERIT has similar bias performances with IEM, whereas phasor and CMM are significantly biased. Fig. 4(a) shows that phasor and CMM favor a larger K. This means FLERIT can be used to resolve histograms obtained by gated FLIM systems as well as TCSPC systems.

IV. Lifetime Resolvability Analysis

To test whether FLERIT can resolve biexponential decays robustly, Monte–Carlo simulations were carried out with $\tau_1 = 1.5$ ns, 1.5 ns $< \tau_2 <$ 6 ns, $(f_{D1}, f_{D2}) = (0.5, 0.5)$, $M = 1024$, and $100 < N_c < 100000$. Other simulation settings

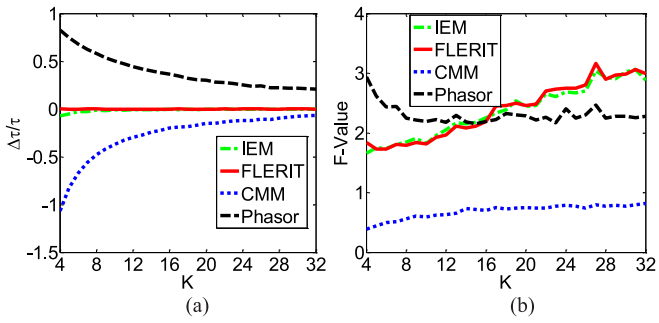

Fig. 4. (a) Bias and (b) F-value plots for different methods in terms of K. $\tau = 3$ ns, the photon number in the first bin is 1000, number of time bins before merging is 1024.

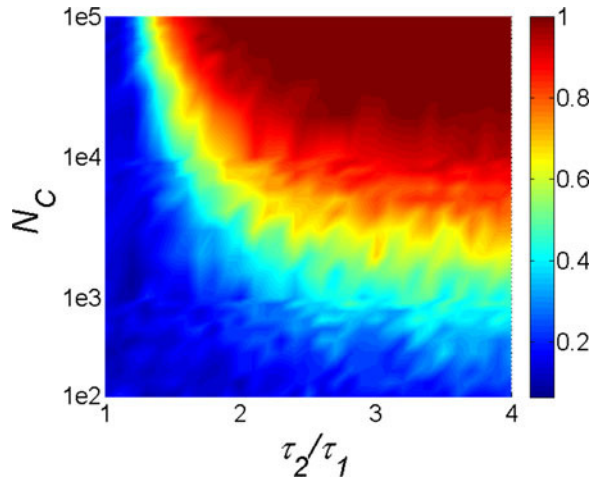

Fig. 5. Probability of resolving τ_1 and τ_2, $\tau_1 = 1.5$ ns, 1.5 ns $< \tau_2 <$ 6 ns, $(f_{D1}, f_{D2}) = (0.5, 0.5)$ and other settings are same as Fig. 3.

are the same as Fig. 2. The histogram was merged into a new one with $K = 8$. The probability of successfully resolving τ_1 and τ_2, P_{Correct}, is defined as the number of correct estimations (the normalized bias is less than 50%) to the number of total simulations. The simulation results are shown in Fig. 5. Simulations show that P_{Correct} is a function of N_c and τ_2/τ_1. Simulations show that FLERIT is unable to resolve lifetimes when $\tau_2/\tau_1 < 1.4$. Fig. 5 also shows that the threshold of N_c is about 10000.

V. Analysis on Synthesized Multidecay FLIM Data

In TCSPC FLIM experiments, the photons collected at each image pixel is limited, either due to the time taken to obtain a viable histogram, limiting for live cell imaging, or due to photobleaching. Pixel binning is, therefore, often applied to improve the signal-to-noise (SNR) of FLIM images at the sacrifice of spatial resolution. To illustrate the FLERIT methodology and advantages, we first use synthesized data with the number of photons limited both 1) without and 2) with pixel binning.

A. Without Pixel Binning

When there is only one lifetime, the number of eigenvectors of the signal space U_S is 1. However, an interesting feature found in FLERIT is that when there are multiple

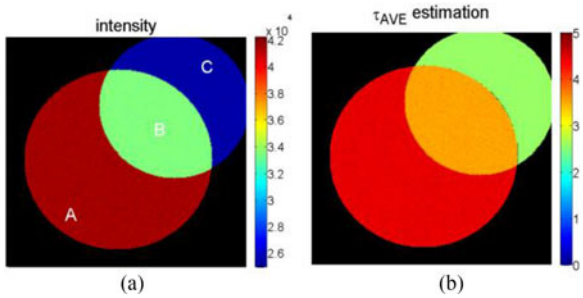

Fig. 6. (a) Intensity and (b) average lifetime image for synthesized data. $\tau_1 = 2$ ns; $\tau_2 = 5$ ns; $(f_{D1}, f_{D2}) = (0.8, 0.2), (0.5, 0.5)$, and (0.2, 0.8) for areas *A*, *B*, and *C*, respectively. The image size is 256 × 256 pixels.

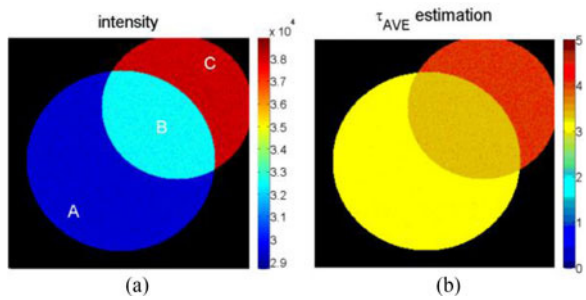

Fig. 7. (a) Intensity and (b) average lifetime image for synthesized triexponential decays. A triexponential decay where $\tau_1 = 2$ ns; $\tau_2 = 3$ ns; $\tau_3 = 5$ ns; $f_{D1} = 0.4, 0.33$, and 0.2, $f_{D2} = 0.4, 0.33$, and 0.2, $f_{D3} = 0.2, 0.34$, and 0.6, for the areas *A*, *B*, and *C*, respectively.

TABLE I
PERFORMANCES OF FLERIT WITHOUT PIXEL BINNING

Area	Exact average lifetime (ns)	Calculated parameters		
		mean (ns)	Standard deviation (ns)	*F* value
Area *A*	4.4	4.45	0.06	1.40
Area *B*	3.5	3.53	0.05	1.43
Area *C*	2.6	2.58	0.03	1.94

TABLE II
PERFORMANCES OF FLERIT FOR SYNTHESIZED TRIEXPONENTIAL DECAYS

Area	Real average lifetime (ns)	Calculated parameters		
		mean (ns)	Standard deviation (ns)	*F* value
Area *A*	3	3.00	0.04	2.06
Area *B*	3.35	3.36	0.04	2.22
Area *C*	4	4.03	0.05	2.55

lifetimes, the eigenvector corresponding to the biggest eigenvalue of R_X is actually a linear combination of all lifetimes when the photon count is limited, i.e., $\tau = f_{D1}\tau_1 + f_{D2}\tau_2 + \cdots$. In Fig. 6(a), assume the histogram in each area is $y(t) = f_{D1}e^{-t/\tau_1} + f_{D2}e^{-t/\tau_2} + \cdots$. The laser repetition rate is set to be 80 MHz ($T = 12.5$ ns).

In the first simulated case, we define the primary and secondary lifetimes $\tau_1 = 2$ ns and $\tau_2 = 5$ ns for all areas and $(f_{D1}, f_{D2}) = (0.8, 0.2)$, (0.5, 0.5), and (0.2, 0.8) for areas *A*, *B*, and *C*, respectively. The image size is 256 × 256 pixels. The photon count at the first bin is 500, and the number of time bins in the histogram is 256 (the histogram was merged into a new one with $K = 8$). The photon count (intensity) of the original data is shown as Fig. 6(a).The averaged lifetime image obtained by FLERIT is shown as Fig. 6(b).

The mean (τ_{AVE}), standard deviation, and *F*-value (normalized precision; $F = 1$ for the ideal case, and $F > 1$ or $F \gg 1$ for realistic FLIM algorithms) of the calculated lifetimes for the three areas are listed in Table I. The precision of the average lifetime is similar to the single-exponential case in Section III.

Consider the second case of a triexponential decay, where $\tau_1 = 2$ ns; $\tau_2 = 3$ ns; $\tau_3 = 5$ ns; $f_{D1} = 0.4$, 0.33, and 0.2, $f_{D2} = 0.4$, 0.33, and 0.2, $f_{D3} = 0.2$, 0.34, and 0.6, for the areas *A*, *B*, and *C*, respectively. The photon count (intensity) of the original data is shown as Fig. 7(a). The averaged lifetime image obtained by FLERIT is shown as Fig. 7(b).

Tables I and II confirm that FLERIT offers an interesting feature similar to the previously reported IEM [33] when it deals with multiexponentials

$$\tau_{\mathrm{AVE}} = \sum_{j=1}^{P} f_{Dj}\tau_j. \tag{14}$$

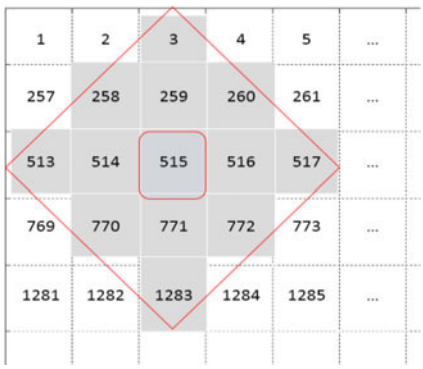

Fig. 8. Binning strategy. The binned data in the square are summed up by all the data in the diamond.

This is a useful feature, as in some applications such as FRET-FLIM experiments [7], (11) can be used to estimate the FRET efficiency. In many biological applications, however, it is desirable to estimate τ_j and $f_{Dj}, j = 1, \ldots, P$ and as previously discussed IEM is only a single exponential approximation.

B. With Pixel Binning

Due to limited photons in the histogram, it is challenging to estimate f_{D1} accurately using (13). Typically pixel binning is used to increase the photon count by trading off the spatial resolution. Using the synthesized data presented in Fig. 6, we adopted a summation-based binning procedure as shown in Fig. 8. The intensity after binning is shown in Fig. 8(a). After binning, τ_1, τ_2, f_{D1}, and f_{D2} can be estimated, and the averaged lifetime can be calculated as shown in Fig. 9(b) using (14).

The performances including the mean, standard deviation, and *F*-value of calculated parameters are listed in Table III.

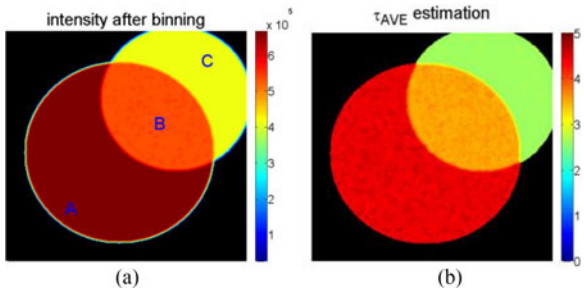

Fig. 9. (a) Intensity and (b) the average fluorescence lifetime images after binning. The simulation setting is the same as Fig. 6.

TABLE III
PERFORMANCES OF FLERIT ON BIEXPONENTIAL DATA AFTER BINNING

Item	Exact value	Simulation results		
		mean	Standard deviation	*F* value
τ_{AVE} of area *A*	4.4 ns	4.40 ns	0.05 ns	2.24
τ_{AVE} of area *B*	3.5 ns	3.52 ns	0.07 ns	3.51
τ_{AVE} of area C	2.6 ns	2.62 ns	0.05 ns	3.05
f_{D1} estimation of area *A*	0.2	0.21	0.07	–
f_{D1} estimation of area *B*	0.5	0.49	0.05	–
f_{D1} estimation of area *C*	0.8	0.79	0.04	–
τ_1 estimation (all *A*, *B*, *C*)	2 ns	1.99 ns	0.46 ns	–
τ_2 estimation (all *A*, *B*, *C*)	5 ns	5.03 ns	0.96 ns	–
τ_1 estimation of area *A*	2 ns	1.99 ns	0.39 ns	–
τ_1 estimation of area *B*	2 ns	2.00 ns	0.14 ns	–
τ_1 estimation of area *C*	2 ns	1.99 ns	0.07 ns	–
τ_2 estimation of area *A*	5 ns	5.02 ns	0.19 ns	–
τ_2 estimation of area *B*	5 ns	5.02 ns	0.21 ns	–
τ_2 estimation of area *C*	5 ns	5.02 ns	0.42 ns	–

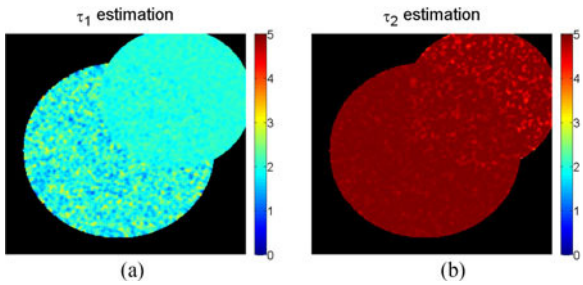

Fig. 10. (a) τ_1 and (b) τ_2 images binning. The simulation setting is the same as Fig. 6.

The table contains more parameters than Table II, as FLERIT resolves all lifetime components and proportional coefficients. The *F*-value is slightly worse than that in Table I, but the FLERIT conducts a blind biexponential analysis solving all four parameters (τ_1, τ_2, f_{D1}, and f_{D2}). The photon efficiency for obtaining the same precision in the *F*-value is 26-fold better if an experiment only requires τ_{AVE}[31] (for some applications, it is not essential to resolve all τ_j and f_{Dj}).

Fig. 10(a) and (b) depicts τ_1 and τ_2 images, respectively. When f_{Dj} is higher, the standard deviation of the corresponding lifetime is lower. Similar to other methods, when f_{D1} approaches 0.0 or 1.0 (nearly single exponential), it requires much more photons to obtain accurate τ_1 and τ_2, respectively.

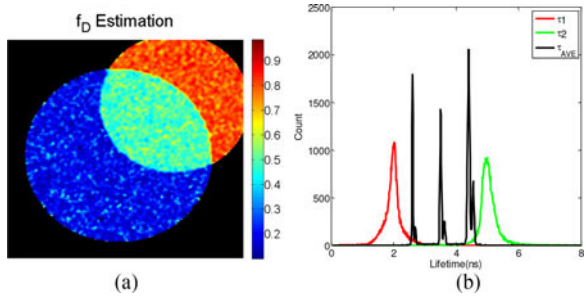

Fig. 11. (a) f_D image and (b) lifetime histograms for τ_1, τ_2, and τ_{AVE} after binning. The simulation setting is the same as Fig. 6.

Fig. 11(a) shows the f_{D1} image after binning. Fig. 11(b) shows lifetime histograms for τ_1, τ_2, and τ_{AVE}. The peak of τ_1 and τ_2 is around 2.01 and 4.94 ns, in good agreement with the exact values. The calculated τ_{AVE} are 2.60, 3.51, and 4.41 ns, again close to the theoretical τ_{AVE} 2.6, 3.5, 4.4 ns in areas *B*, *C*, and *A* as shown in Fig. 6(a). The SNR of τ_{AVE} is much better than each individual τ_j and f_{Dj}. The ratio of the measurement window to τ_2(12.5/5 ns), is only 2.5, much smaller than the recently proposed biexponential algorithms [48], indicating that the duty cycle of the laser repetition can be higher giving better photon efficiency.

VI. EXPERIMENTAL DETAILS

To test FLERIT on real data, FLIM experiments were carried out on HeLa cells ubiquitously expressing EGFP using a commercial scanning confocal FLIM system

A. Experimental Setup

Data were acquired using a Leica SP5 scanning confocal microscope fitted with a PicoHarp 300 TCSPC module. Excitation was with a tunable white light laser operating at 488 nm and 40 MHz. Detection was with a single-channel MPD SPAD, collecting the majority of EGFP emission. All images where Nyquist sampled, 512 × 512 pixels, and with predefined total image integration times set to 10, 60, 180, and 600 s.

B. Sample Preparation

HeLa cells were plated onto 25-mm glass coverslips previously coated with 50-μg/ml poly-D-Lysine hydrobromide (UV irradiated for sterility) and grown for 24 h at 37 °C and 5% CO_2. Cells were cultured in DMEM (Gibco, 31053) supplemented with 100-U/ml penicillin, 100-μg/ml streptomycin (Gibco, 15140), 10% heat-inactivated foetal bovine serum (Gibco, 10500064), 1X Glutamax (Gibco, 35050), and 1-mM sodium pyruvate (Gibco, 11360). Following 24 h growth, cells were transfected using Turbofect transfection reagent (Thermo Scientific, R0531) with 2-μg pEGFP-N1, a discontinued Clontech plasmid encoding enhanced green fluorescent protein, and incubated for a further 24 h at 37 °C and 5% CO_2 to allow expression of the encoded EGFP. Cells were washed with 1X phosphate buffered saline, fixed with 4% paraformaldehyde, and blocked with 50-mM ammonium chloride prior to mounting on

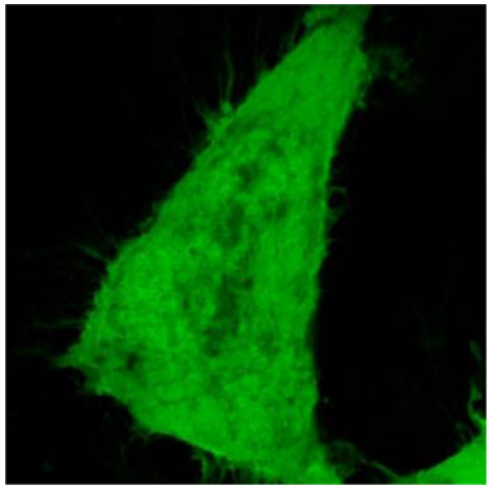

Fig. 12. Epifluorescence image.

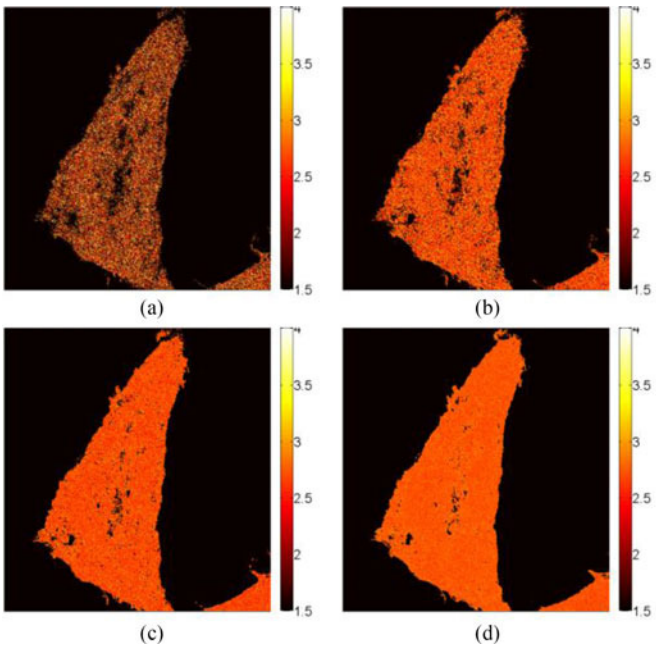

Fig. 13. τ_{AVE} images for the acquisition of (a) 10 s, (b) 60 s, (c) 180 s, and (d) 600 s.

slides with MOWIOL 4-88 and allowing to set overnight before imaging.

C. Experiment Data Analysis

Fig. 12 shows the epifluorescence image an example cell with ubiquitously expressed EGFP. Fig. 13(a)–(d) shows the average fluorescence lifetime image for the acquisition time of 10, 60, 180, and 600 s (the maximum photon count are 54, 251, 756, and 1939, respectively). The figures show that the deviations of the lifetime decrease as the acquisition time is increased. Fig. 14(a)–(d) shows the histograms of τ_{AVE} for the acquisition time of 10, 60, 180, and 600 s. Fig. 14 shows that the standard deviation can be improved with a longer acquisition and it is inversely proportional to the square root of the acquisition, in agreement with the conclusion given in [28]. Fig. 15(a)–(d)

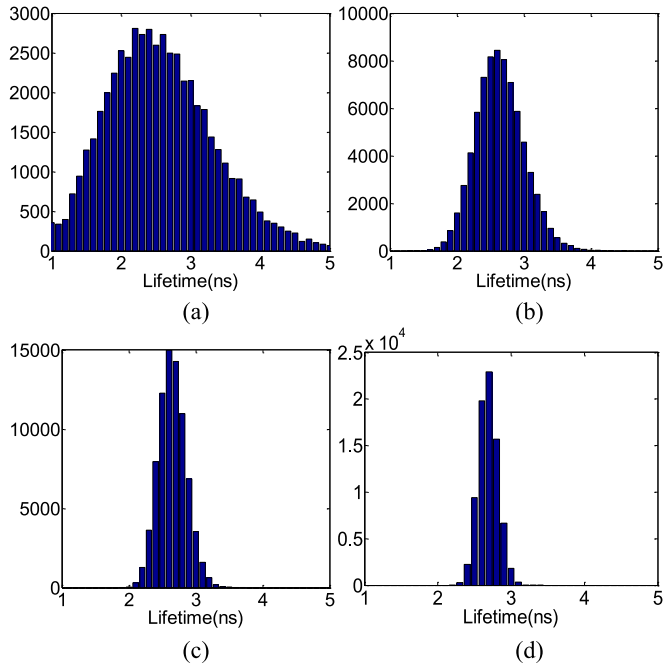

Fig. 14. τ_{AVE} histograms for the acquisition of (a) 10 s, (b) 60 s, (c) 180 s, and (d) 600 s.

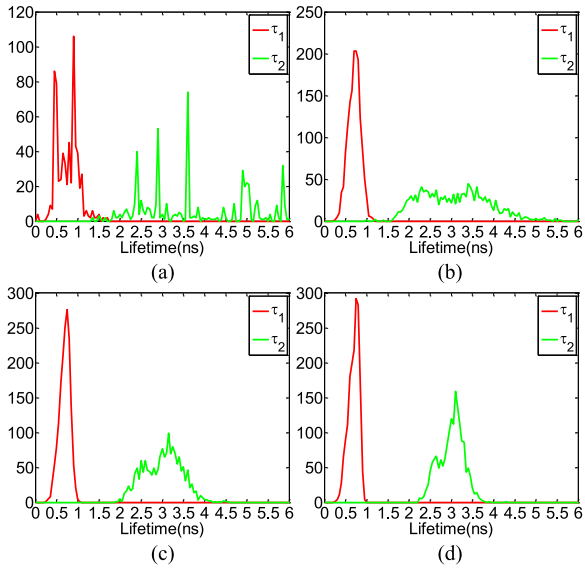

Fig. 15. τ_1 and τ_2 histograms of for the acquisition of (a) 10 s, (b) 60 s, (c) 180 s, and (d) 600 s.

shows the histograms of τ_1 and τ_2 for different acquisitions. The biexponential ingredient is 1.58%, 2.12%, 2.12%, and 2.21%, respectively, for 10, 60, 180, and 600 s. The peaks of τ_1 and τ_2 histograms are located at around 850 ps and 3 ns. The average lifetime is about 2.8 ns, in accordance with [49].

D. Time Consumption of the Data Analysis

We have run the data analysis using MATLAB on DELL Optiplex 7010 desktop. For a 512 × 512 image, it takes 26.7 s. If FLERIT is implemented in a hardware similar to [31], the computational burden can be further decreased by adopting the

fast multistage Wiener filtering method [50], Lanczos algorithm [51], and propagator method [52]. With more and more hardware multipliers or intellectual property cores embedded in DSP processors and FPGA circuits, the proposed method can be realized in such embedded systems for real-time applications.

VII. Conclusion

In this paper, we proposed a new method called FLERIT. The derivations of FLERIT have been carried out by introducing a signal model. The performances of FLERIT were demonstrated on both synthesized and experimental data. The new method does not require any prior information and it can be applied to both gated CCDs and TCSPC systems with limited number of timing channels. For more accurate analysis, the model can be extended to include the IRF, but it is an independent work not covered in this paper. Simulations and experiments show that FLERIT can provide single-exponential average fluorescence lifetimes similar to the previously reported IEM method or multiple exponential analysis. FLERIT can extract fluorescence lifetimes by only a few time gates, which can reduce the data throughput between a parallel TCPSC front-end and a data analyzing system. The computation burden of FLERIT is much less than traditional fitting methods making it suitable for implementations in embedded systems.

References

[1] M. Elangovan *et al.*, "Nanosecond fluorescence resonance energy transfer-fluorescence lifetime imaging microscopy to localize the protein interactions in a single living cell," *J. Microsc.*, vol. 205, pp. 3–14, 2002.

[2] P. I. Bastiaens and A. Squire, "Fluorescence lifetime imaging microscopy: Spatial resolution of biochemical processes in the cell," *Trends Cell Biol.*, vol. 9, pp. 48–52, 1999.

[3] S. Coda *et al.*, "Fluorescence lifetime spectroscopy of tissue autofluorescence in normal and diseased colon measured ex vivo using a fiber-optic probe," *Biomed. Opt. Exp.*, vol. 5, pp. 515–538, 2014.

[4] T. S. Blacker *et al.*, "Separating NADH and NADPH fluorescence in live cells and tissues using FLIM," *Nature Commun.*, vol. 5, pp. 1–9, 2014.

[5] M. Nobis *et al.*, "Intravital FLIM-FRET imaging reveals dasatinib-induced spatial control of src in pancreatic cancer," *Cancer Res.*, vol. 73, pp. 4674–4686, 2013.

[6] C. N. Medine *et al.*, "Munc18-1 prevents the formation of ectopic SNARE complexes in living cells," *J. Cell Sci.*, vol. 120, pp. 4407–4415, 2007.

[7] E. Fišerová and M. Kubala, "Mean fluorescence lifetime and its error," *J. Luminescence*, vol. 132, pp. 2059–2064, Aug. 2012.

[8] T. Omer *et al.*, "Reduced temporal sampling effect on accuracy of time-domain fluorescence lifetime Förster resonance energy transfer," *J. Biomed. Opt.*, vol. 19, pp. 086023-1–086023-9, 2014.

[9] S. Burri *et al.*, "Architecture and applications of a high resolution gated SPAD image sensor," *Opt. Exp.*, vol. 22, pp. 17573–17589, Jul. 14, 2014.

[10] R. M. Field *et al.*, "A 100 fps, time-correlated single-photon-counting-based fluorescence-lifetime imager in 130 nm CMOS," *IEEE J. Solid-State Circuits*, vol. 49, no. 4, pp. 867–880, Apr. 2014.

[11] C. Veerappan *et al.*, "A 160 × 128 single-photon image sensor with on-pixel 55 ps 10b time-to-digital converter," in *Proc. IEEE Int. Solid-State Circuits Conf. Dig. Tech. Papers*, 2011, pp. 312–314.

[12] L. Rosso and V. C. Fernicola, "Time- and frequency-domain analyses of fluorescence lifetime for temperature sensing," *Rev. Sci. Instrum.*, vol. 77, pp. 034901–1–034901-6, 2006.

[13] P. Roudot *et al.*, "Lifetime map reconstruction in frequency-domain fluorescence lifetime imaging microscopy," in *Proc. IEEE 19th Int. Conf. Image Process.*, 2012, pp. 2537–2540.

[14] P. Vita *et al.*, "Deep-ultraviolet light-emitting diodes for frequency domain measurements of fluorescence lifetime in basic biofluorophores," *Appl. Phys. Lett.*, vol. 87, pp. 084106–1–084106-3, 2005.

[15] M. Zhao *et al.*, "Parallel excitation-emission multiplexed fluorescence lifetime confocal microscopy for live cell imaging," *Opt. Exp.*, vol. 22, pp. 10221–10232, May 5, 2014.

[16] H. Yu and D. D.-U. Li, "Fluorescence lifetime extraction algorithm based on multiple signal classification," *Electron. Lett.*, vol. 51, pp. 81–83, 2015.

[17] L. Turgeman and D. Fixler, "Photon efficiency optimization in time-correlated single photon counting technique for fluorescence lifetime imaging systems," *IEEE Trans. Biomed. Eng.*, vol. 60, no. 6, pp. 1571–1579, Jun. 2013.

[18] S. P. Poland *et al.*, "A high speed multifocal multiphoton fluorescence lifetime imaging microscope for live-cell FRET imaging," *Biomed. Opt. Exp.*, vol. 6, pp. 277–296, Jan. 2, 2015.

[19] J. F. Hauer *et al.*, "Initial results in Prony analysis of power system response signals," *IEEE Trans. Power Syst.*, vol. 5, no. 1, pp. 80–89, Feb. 1990.

[20] J. L. Rinnenthal *et al.*, "Parallelized TCSPC for Dynamic intravital fluorescence lifetime imaging: Quantifying neuronal dysfunction in neuroinflammation," *PLoS One*, vol. 8, p. e60100, 2013.

[21] S. P. Poland *et al.*, "Time-resolved multifocal multiphoton microscope for high speed FRET imaging in vivo," *Opt. Lett.*, vol. 39, pp. 6013–6016, 2014.

[22] M. I. Rowley *et al.*, "Bayesian analysis of fluorescence lifetime imaging data," *Proc. SPIE*, vol. 7903, pp. 790325-1–790325-12, 2011.

[23] R. Swaminathan and N. Periasamy, "Analysis of fluorescence decay by the maximum entropy method: Influence of noise and analysis parameters on the width of the distribution of lifetimes," *Proc. Indian Acad. Sci., Chem. Sci.*, vol. 108, pp. 39–49, Feb. 1, 1996.

[24] P. Hall and B. Selinger, "Better estimates of exponential decay parameters," *J. Phys. Chem.*, vol. 85, pp. 2941–2946, Oct. 1, 1981.

[25] M. Maus *et al.*, "An experimental comparison of the maximum likelihood estimation and nonlinear least-squares fluorescence lifetime analysis of single molecules," *Analytical Chem.*, vol. 73, pp. 2078–2086, May 1, 2001.

[26] S. Pelet *et al.*, "A fast global fitting algorithm for fluorescence lifetime imaging microscopy based on image segmentation," *Biophys. J.*, vol. 87, pp. 2807–2817, 2004.

[27] G.-H. Kim *et al.*, "Single-molecule analysis and lifetime estimates of heterogeneous low-count-rate time-correlated fluorescence data," *Appl. Spectrosc.*, vol. 65, pp. 981–990, 2011.

[28] S. Zahner *et al.*, "Fluorescence lifetime imaging microscopy and polar-plot analysis of gallium selenide crystals," *J. Appl. Phys.*, vol. 115, pp. 043504–1–043504-7, 2014.

[29] A. Leray *et al.*, "Three-dimensional polar representation for multispectral fluorescence lifetime imaging microscopy," *Cytometry Part A*, vol. 75A, pp. 1007–1014, 2009.

[30] Z. Zhang *et al.*, "Prony's method for exponential lifetime estimations in fluorescence based thermometers," *Rev. Sci. Instrum.*, vol. 67, pp. 2590–2594, 1996.

[31] D.-U. Li *et al.*, "Real-time fluorescence lifetime imaging system with a 32 × 32 0.13 μm CMOS low dark-count single-photon avalanche diode array," *Opt. Exp.*, vol. 18, pp. 10257–10269, May 10, 2010.

[32] D. D. U. Li *et al.*, "Video-rate fluorescence lifetime imaging camera with CMOS single-photon avalanche diode arrays and high-speed imaging algorithm," *J. Biomed. Opt.*, vol. 16, pp. 096012–1–096012-12, 2011.

[33] D. D.-U. Li *et al.*, "Time-domain fluorescence lifetime imaging techniques suitable for solid-state imaging sensor arrays," *Sensors*, vol. 12, pp. 5650–5669, 2012.

[34] P. R. Barber *et al.*, "Global and pixel kinetic data analysis for FRET detection by multi-photon time-domain FLIM," *Proc. SPIE*, vol. 5700, pp. 171–181, 2005.

[35] D.-U. Li *et al.*, "Hardware implementation algorithm and error analysis of high-speed fluorescence lifetime sensing systems using center-of-mass method," *J. Biomed. Opt.*, vol. 15, pp. 017006-1–017006-10, 2010.

[36] D. M. Grant *et al.*, "High speed optically sectioned fluorescence lifetime imaging permits study of live cell signaling events," *Opt. Exp.*, vol. 15, pp. 15656–15673, Nov. 26, 2007.

[37] R. M. Ballew and J. N. Demas, "An error analysis of the rapid lifetime determination method for the evaluation of single exponential decays," *Anal. Chem.*, vol. 61, pp. 30–33, Jan. 1, 1989.

[38] R. Woods *et al.*, "Transient digitizer for the determination of microsecond luminescence lifetimes," *Anal. Chem.*, vol. 56, pp. 1395–1400, 1984.

[39] S. P. Chan *et al.*, "Optimized gating scheme for rapid lifetime determinations of single-exponential luminescence lifetimes," *Anal. Chem.*, vol. 73, pp. 4486–4490, 2001.

[40] A. Leray *et al.*, "827Spatio-temporal quantification of FRET in living cells by fast time-domain FLIM: A comparative study of non-fitting methods," *PLoS One*, vol. 8, p. e69335, 2013.
[41] G. Mao *et al.*, "Wireless sensor network localization techniques," *Comput. Netw.*, vol. 51, pp. 2529–2553, 2007.
[42] H. Kim and M. Viberg, "Two decades of array signal processing research," *IEEE Signal Mag.*, vol. 13, no. 4, pp. 67–94, Jul. 1996.
[43] D. L. Hall and J. Llinas, "An introduction to multisensor data fusion," *Proc. IEEE*, vol. 85, no. 1, pp. 6–23, Jan. 1997.
[44] E. G. Novikov *et al.*, "Linear algorithms for stretched exponential decay analysis," *Opt. Commun.*, vol. 166, pp. 189–198, 1999.
[45] M. Y. Berezin and S. Achilefu, "Fluorescence lifetime measurements and biological imaging," *Chem. Rev.*, vol. 110, pp. 2641–2684, 2010.
[46] R. A. Horn and C. R. Johnson, *Matrix Analysis*. Cambridge, U.K.: Cambridge Univ. Press, 2012.
[47] H. C. Gerritsen *et al.*, "Fluorescence lifetime imaging in scanning microscopes: Acquisition speed, photon economy and lifetime resolution," *J. Microsc.*, vol. 206, pp. 218–224, 2002.
[48] D. D.-U. Li *et al.*, "Fast bi-exponential fluorescence lifetime imaging analysis methods," *Opt. Lett.*, vol. 40, pp. 336–339, Feb. 1, 2015.
[49] G. Striker *et al.*, "Photochromicity and fluorescence lifetimes of green fluorescent protein," *J. Phys. Chem. B*, vol. 103, pp. 8612–8617, 1999.
[50] J. S. Goldstein *et al.*, "A multistage representation of the Wiener filter based on orthogonal projections," *IEEE Trans. Inf. Theory*, vol. 44, no. 7, pp. 2943–2959, Nov. 1998.
[51] Z. Bai, "Krylov subspace techniques for reduced-order modeling of large-scale dynamical systems," *Appl. Numer. Math.*, vol. 43, pp. 9–44, 2002.
[52] S. Marcos *et al.*, "The propagator method for source bearing estimation," *Signal Process.*, vol. 42, pp. 121–138, 1995.

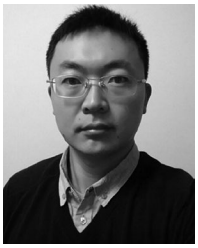

Hongqi Yu received the B.S., M.S., and Ph.D. degrees from the National University of Defense Technology (NUDT), Changsha, China, in 2000, 2003, and 2007, respectively.

He is an Associate Professor at NUDT. He was an Academic Visitor at Center for Biophotonics, University of Strathclyde, Glasgow, U.K., from June 2014 to July 2015. His research interests focus around signal processing, SPAD based FLIM system and embedded system.

Rebecca Saleeb received the B.Sc.(Hons.) degree in cell biology from Durham University, Durham, U.K., in 2009, which incorporated an industrial trainee scientist placement with Pfizer Animal Health from 2007–2008. She received the Master's degree in biotechnology from the University of Queensland, Queensland, Australia, in 2011 while researching novel point of care diagnostics for infectious diseases. She is currently working toward the Ph.D. degree in biophysics within the Advanced Microscopy Group, Heriot Watt University, Edinburgh, U.K.

Her research interests include the use and development of bioimaging technologies to detect protein interactions and specifically deepen understanding of the molecular mechanisms driving cell survival pathways.

Paul Dalgarno received the M.Phys. and Ph.D. degrees in physics from Heriot-Watt University, Edinburgh, U.K., in 2001 and 2005, respectively.

Until 2010, he researched self-assembled quantum dot systems at Heriot-Watt, specialising in time resolved spectral measurements. In 2010, he moved to the University of St. Andrews, U.K., to research biopolymer folding and organic polymers. In 2012, he returned to Heriot-Watt University as an Assistant Professor, leading the Advanced Microscopy Group. His research interests include high resolution, multispectral, and 3D microscopy for the life sciences and clinical applications.

Dr. Dalgarno is a Member of the Institute of Physics and a chartered physicist.

David Li received the Ph.D. degree in electrical engineering from National Taiwan University, Taipei, Taiwan, in 2001.

He is a Senior Lecturer, Centre for Biophotonics, University of Strathclyde, Glasgow, U.K. He worked at the Industrial Technology Research Institute, Taiwan, as an R&D Engineer on optical and wireless communication transceivers and transferred knowledge to industry. From 2007, he worked at the University of Edinburgh on the EU projects MEGAFRAME and METOXIA to develop CMOS single-photon avalanche diode (SPAD) based fluorescence lifetime imaging (FLIM) & spectroscopy systems. From 2011 to 2013, he was a Lecturer in biomedical engineering, University of Sussex, working on various electrical impedance tomography/spectroscopy and FLIM projects. He has expertise in mixed-signal circuits, FLIM systems and analysis, computing and numerical analysis, and optical communications. His current research interests include the applications of SPAD sensors for fluorescence imaging and spectroscopy, GPU computing techniques for image analysis, and FLIM-FRET techniques for cancer diagnosis.